Available online at www.sciencedirect.com
SCIENCE DIRECT®
Journal of Organometallic Chemistry 683 (2003) 368–378
Journal of Organometallic Chemistry
www.elsevier.com/locate/jorganchem

Chemistry of the 1,3,5,7-octatetraynediyl carbon rod end-capped by two electron-rich (η^5-C_5Me_5)(η^2-dppe)Fe groups

Françoise Coat [a], Frederic Paul, * [a], Claude Lapinte [a,*], Loic Toupet [b], Karine Costuas [c], Jean-François Halet, * [c]

[a] *Organométalliques et Catalyse, Chimie et Electrochimie Moléculaire, Institut de Chimie de Rennes, UMR CNRS 6509, Université de Rennes 1, Campus de Beaulieu, F-35042 Rennes Cedex, France*
[b] *Groupe Matière Condensée et Matériaux, UMR 6626, Université de Rennes 1, Campus de Beaulieu, F-35042 Rennes Cedex, France*
[c] *Laboratoire de Chimie du Solide et Inorganique Moléculaire, Institut de Chimie de Rennes, UMR CNRS 6511, Université de Rennes 1, Campus de Beaulieu, F-35042 Rennes Cedex, France*

Received 26 May 2003

Abstract

The synthesis of the organoiron complex [(η^5-C_5Me_5)(η^2-dppe)Fe–C≡C–C≡C–C≡C–C≡C–Fe(η^2-dppe)(η^5-C_5Me_5)] (**2**, dppe = 1,2-bis(diphenylphosphino)ethane) is reported with its full spectroscopic characterizations (^{1}H-, ^{31}P-, and ^{13}C-NMR, IR, Raman, UV–vis and ^{57}Fe Mössbauer). The X-ray analysis of **2** shows that the molecule adopts a geometry very close to the *anti* conformation in the solid state. The shortening of the Fe–C bond distance associated with the increase in the number of carbon atoms suggests some cumulenic contribution to the description of the electronic structure of the all-carbon bridge. The ^{13}C-NMR, ^{57}Fe Mössbauer data and theoretical calculations confirm this trend and indicate that the cumulenic contribution is significant in the vicinity of the metal center but vanishes in the middle of the carbon rod. Vibrational spectroscopy carried out on the single crystals of [(η^5-C_5Me_5)(η^2-dppe)Fe–C≡C–C≡C–Fe(η^2-dppe)(η^5-C_5Me_5)] (**1**) and **2** and on solutions of these compounds indicates that the C≡C bond stretching mode is not very sensitive to the relative orientation of the terminal endgroups. The electronic structure of the titled compound has been investigated using density functional theory. The geometrical changes occurring upon elongation of the carbon chain were nicely reproduced and interpreted. Time-dependant density functional theory calculations have been performed to rationalize the optical spectra.

Keywords: Organoiron complex; 1,3,5,7-Octatetraynediyl carbon rod; ^{57}Fe Mössbauer; NMR; All-carbon chain

1. Introduction

In recent years, there has been rapidly increasing interest in organometallic compounds with long all-carbon chains. Bimetallic complexes with poly-ynediyl bridges, M–(C≡C)$_n$–M, constitute the most fundamental class of carbon-based molecular wires and they have been proposed for the construction of nanoscale electronic devices [1–5]. In addition, the carbon chain possesses a fascinating ability to mediate magnetic interaction when the metal ends act as spin carriers [6]. Using a variety of transition metal capping groups, families of M–(C≡C)$_n$–M complexes have been obtained with n ranging from 2 to 10 [7–12]. These compounds usually become less stable as the carbon chains are extended and so far have resisted crystallization for X-ray diffraction analyses. However, the stability of these molecules can be increased using electron-withdrawing or moderate electron-donating termini. As a result, several examples of compounds containing C_8–C_{16} carbon chains have been X-ray characterized but unfortunately, most of these compounds are not redox-active [13–16].

Recently, we have been able to carry out an X-ray diffraction study on the known [(η^5-C_5Me_5)(dppe)Fe–C≡C–C≡C–Fe(dppe)(η^5-C_5Me_5)] (**1**) complex [17], and we now report the molecular structure of its homologue with a C_8 carbon chain [(η^5-C_5Me_5)(ddpe)Fe–C≡C–C≡

* Corresponding authors. Tel./fax: +33-2-2323-5963.
E-mail address: claude.lapinte@univ-rennes1.fr (C. Lapinte).

0022-328X/03/$ - see front matter © 2003 Elsevier B.V. All rights reserved.
doi:10.1016/S0022-328X(03)00709-5

C–C≡C–C≡C–Fe(dppe)(η^5-C_5Me_5)] (**2**). In addition, we also report: (i) the experimental details for the synthesis of this complex, (ii) a comparative conformational analysis of **1** and **2** carried out on the basis of IR, Raman and ^{31}P-NMR studies, (iii) a discussion on the electronic structure of the all-carbon chain in the binuclear organometallic Fe–$(C\equiv C)_n$–Fe complexes and its evolution when n increases supported by the X-ray study, ^{13}C-NMR and ^{57}Fe Mössbauer spectroscopies and selected literature data, and (iv) the effect of the carbon chain length on the electronic transitions measured by UV–visible spectroscopy. Part of this work has been previously communicated [18].

2. Results and discussion

2.1. Synthesis

We have recently found an efficient preparation of the butadiynyl complex (C_5Me_5)(dppe)Fe($C\equiv C$–$C\equiv CSiMe_3$) (**3**) in one-step from (C_5Me_5)Fe(dppe)Cl and trimethylsilylbutadiyne [19]. The subsequent desilylation of **3** was achieved with a catalytic amount of Bu_4NF in THF. The complex (C_5Me_5)(dppe)Fe($C\equiv C$–$C\equiv CH$) (**4**) was obtained in 95% yield as an orange-red powder [20]. Oxidative coupling of **4** with $Cu(OAc)_2$ in pyridine at 45 °C in presence of one equivalent of DBU gave the binuclear complex (C_5Me_5)(dppe)Fe($C\equiv C$–$C\equiv C$–$C\equiv C$–$C\equiv C$)Fe(dppe)(C_5Me_5) (**2**) in 80% yield as a red powder (Scheme 1).

2.2. Crystal structure of 2

Single crystals of **2** could be grown as large ruby-red cubic shaped prisms by slow diffusion of acetone into a dichlomethane solution of complex **2** and the corresponding solid-state structure could be solved. Alternatively, single crystals of **2**·CH_2Cl_2 containing a dichloromethane molecule as solvate could also be obtained in the same way. Given that the dimensions of the unit cells were comparable for **2** and **2**·CH_2Cl_2 and given that the conformation of the molecule did not change, resolution of the latter structure was not continued. The molecular structure for the non-solvated

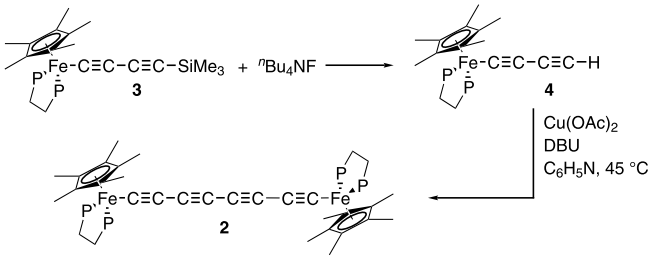

Scheme 1.

complex is shown in Fig. 1. Crystallographic data for **2** are summarized in Table 1, whereas selected bond distances and angles are given in Table 2. The distances and angles of the Fe–C_8–Fe assembly are highlighted in Plate 1. General features, such as the formally octahedral geometry at each metal, are as expected from related structures in this series [20,21]. All bond lengths and angles for **2** fall into previously established ranges [1]. As expected, the Fe–C_α bonds (1.862 and 1.864 Å) are shorter than iron–C(sp^3) bonds (2.075 Å) [17] and even shorter than those of the C_4 analogue previously reported (1.884 and 1.889 Å) [17]. The bonding within the Fe–C_8–Fe core resembles also these reported for the Fe–C_4–Fe core, as shown for the triple C≡C bonds (1.222, 1.199, 1.228 and 1.210 Å vs. 1.220 and 1.220 Å), and the single C–C carbon–carbon bonds (1.361, 1.369 and 1.364 Å vs. 1.374 Å). The average values for the C≡C and C–C bond lengths are 1.215 and 1.366 Å, respectively. In the shorter analogue **1**, both the C≡C and C–C bond lengths are slightly longer (1.220 and 1.374 Å, respectively). The bond length alternation defined by the difference between averaged single and triple carbon–carbon bond distances tends to decrease when the number of carbon atoms increases in the polyynediyl spacer (**2**, 0.151; **1**, 0.154 Å) [7].

Using the C_5Me_5 ligand on each endgroup as a reference point for analyzing the conformation about the all-carbon ligand and the centroids to define a torsion angle (θ), with 180° and 0° corresponding to *anti* and *syn* arrangements, respectively (Scheme 2), we see that compound **3** shows a geometry very close to the *anti* conformation ($\theta = 178.2°$). This arrangement of the terminal building blocks constitutes a notable difference from the FeC_4Fe analog which exhibits an almost *gauche* arrangement of the terminal ends ($\theta = 78.9°$). However, as both compounds crystallize in the same space group ($P2_1/c$), packing effects are likely to be the origin of the different conformations. On the other hand, **1**·PF_6 exhibits a typical *anti* conformation ($\theta = 180°$), as expected from the crystallographic inversion center located at the middle of the bridge [8].

The Fe–$(C\equiv C)_4$–Fe linkage can be viewed as a carbon rod. The two iron atoms are separated by 12.65 Å. The sum of the bond distances of the bis(iron) octatetraynediyl assembly is 12.68 Å indicating that the rod is only very weakly distorted. The FeC_8Fe linkage in **2** deviates somewhat from linearity and shows a slight S-shape (Fig. 1). However, the Fe–C≡C angles (176.3° and 177.9°) are similar to the corresponding ones observed in the FeC_4Fe analogue **1** (178.8° and 174.6°) and remain close to 180°. The average bond angle (177.2°) is greater in **2** than in **1** (176.4°). This very slight bending is probably electronic in origin (see Section 2.7). Small structural deformations of the carbon chain have also been attributed to the packing effects in the related complexes [7,17,22].

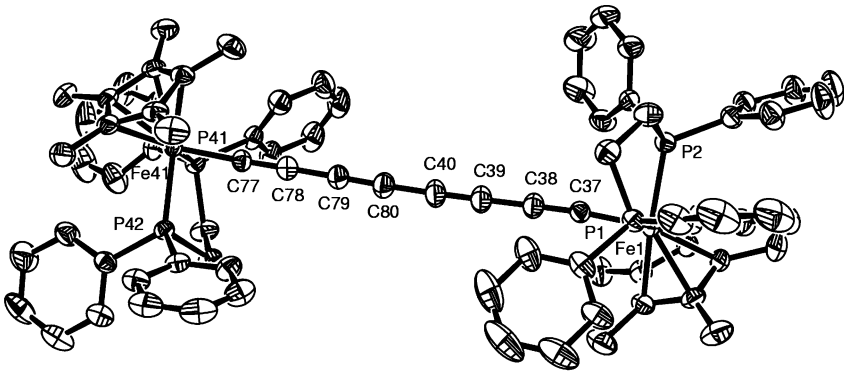

Fig. 1. Molecular structure of **2** drawn at the 50% probability level.

As shown in Fig. 2, the closest intermolecular interactions between non-hydrogen atoms are found between the carbon chains and atoms of the organoiron terminal ends which separate, the all-carbon fragments from each other in the solid state. The closest interactions between C_8 carbon rods are larger than 12 Å (C38–C′39 = 12.7 Å, C37–C′39 = 12.5 Å, C37–C′ = 12.2 Å). In addition, observation of unit cells with similar dimensions for **2** and **2**·CH_2Cl_2 are consistent with the formation of small cavities in the lattice (see Fig. 2). Probably, such an arrangement of the molecule in the crystal favors the high stability of the solid samples. It is noteworthy that crystals grown from a CH_2Cl_2 solution of **2** by slow diffusion of pentane provided a much more sensitive material. These crystals are stable and diffract the X-rays, but after a short period of time (15–20 min) under X-ray irradiation even at low temperature (110 K), they collapsed to non-crystalline material and the diffraction stopped.

The X-ray structure determination of molecules containing poly-ynediyl fragments often provides constant bond distances and distortions are usually attributed to packing effects [23–25]. In addition, the acetylenic carbon atoms often present large anisotropies, which limit accurate determination of the bond lengths [23]. More interesting, the shortening of the Fe–C distances as the poly-ynediyl chain length increases constitutes an important feature. A similar trend was also observed by Akita et al. for the Fe–$(C{\equiv}C)_n$–Fe linkages ($n = 1$, 2 and 6), in the Fp* series (Table 3). These structural changes may be rationalized by considering an increasing weight of the cumulenic-like mesomers B and C (Scheme 3) in the bonding description of the all-carbon bridge. Moreover, their weight would increase not only with the electron-releasing effect of the endgroups, but also with the number of carbons in the poly-ynediyl chain. Spectroscopic data reported below indicate that the retrodonation should contribute significantly to the electronic structure of **2**.

2.3. NMR spectroscopy

The ^{1}H-NMR spectrum of **2** displays a sharp singlet for the (η^5-C_5Me_5) resonance, whereas two multiplets are observed at δ 2.45 and 1.79 ppm for the non-equivalent protons of CH_2 groups of the dppe ligand. The ^{31}P spectrum shows a unique sharp singlet corresponding to the dppe ligand (δ, 98.5 ppm) and no broadening was observed at low temperatures indicating that the two organometallic fragments bound to the all-carbon chain rotate freely. In contrast, the sharp signal observed at 293 K (δ, 100.9 ppm) in the ^{31}P-NMR spectrum of a freshly prepared CD_2Cl_2 solution of the Fe–C_4–Fe homologue **1** broadens as the temperature decreases and the coalescence was observed at 223 K (300 MHz, Fig. 3). Below this temperature, two singlets arose from the noise and are distinctly observed at 193 K (δ, 99.0 and 101.9 ppm) with an integration ratio close to 1. The free energy for the rotation barrier in CD_2Cl_2 is 28.2 kJ mol^{-1} (6.74 kcal mol^{-1}) Rotation of the terminal groups about the iron–C_4–iron axis gives rise to different conformers which slowly interconvert in solution as shown in Scheme 2. In some of these conformers, the magnetic environment of the phosphorus nuclei should be different enough to give resonances with different chemical shifts, but the four atoms of phosphorus are magnetically equivalent for each conformer.

It is clear that the rotation barrier is steric in origin since free rotation is observed for **2**. Using CHEM-3D software and the data obtained from the X-ray study of **1**, an analysis of the close contacts between carbon atoms of the two endgroups upon rotation of the two moieties of the molecule about the central carbon atoms C_β–C'_β shows that the distance between the phenyl rings of the two dppe ligands would be as short as 1.55 Å in the *syn* conformer. The shortest distances determined between unbound carbon atoms in the *anti* and *gauche* conformers are above 5 Å. It is unlikely that the *syn* conformer could exist in solution of **1**. It is also of

Table 1
Crystallographic data for **2**

Molecular formula	$C_{80}H_{78}Fe_2P_4$
Molecular weight	1275.00
Temperature (K)	293(2)
Crystal system	Monoclinic
Space group	$P2_1/c$
Unit cell dimensions	
a (Å)	18.0042(5)
b (Å)	18.502(5)
c (Å)	20.698(8)
α (°)	99.11(2)
V (Å^3)	6822(3)
Z	4
D_{calc} (g cm^{-3}) (294 K)	1.241
Absorption coefficient (mm^{-1})	0.562
$F(0\,0\,0)$	2680
Crystal size (mm^3)	0.24 × 0.21 × 0.15
Diffractometer	CAD4 NONIUS
Radiation (Å)	Mo–K_α (0.71073)
Data collection method	$\omega/2\theta$
t_{max}/measure (s)	60
Index ranges	$0 \le h \le 23$, $0 \le k \le 18$; $-26 \le l \le 26$
θ range	1.48–26.97
Reflections measured	13874
Independent reflections	13474
Observed data [$I > 2\sigma(I)$]	8111
No. of variables	776
R_{int} (from merging equiv. reflections)	0.0165
Final R	0.044 [$R_w = 0.111$]
R indices (all data)	0.0905 [$R_w = 0.1097$]
Goodness-of-fit on F^2	0.975
Largest difference peak and hole (e Å^{-3})	0.394 and −0.336

Table 2
Selected distances (Å) and angles (°) for **2**

Bond lengths	
Fe1–P1	2.1918(10)
Fe1–P2	2.1979(10)
Fe4–P41	2.1943(9)
Fe4–P42	2.1884(10)
Fe1–C37	1.864(3)
Fe4–C77	1.862(3)
C37–C38	1.222(4)
C38–C39	1.369(4)
C39–C40	1.199(4)
C40–C80	1.364(4)
C80–C79	1.210(4)
C79–C78	1.361(4)
C78–C77	1.228(4)
Fe1–C_5Me_5 (centroid)	1.743
Fe2–C_5Me_5 (centroid)	1.746
Fe1–Fe2	12.655
Bond angles	
P1–Fe1–P2	85.59(4)
P1–Fe1–C37	81.87(9)
P2–Fe1–C37	88.46(9)
P41–Fe4–P42	85.60(4)
P41–Fe4–C77	85.92(9)
P42–Fe4–C77	84.02(9)
Fe1–C37–C38	176.3(4)
C37–C38–C39	174.6(4)
C38–C39–C40	177.7(4)
C39–C40–C80	178.3(4)
C40–C80–C79	177.9(4)
C78–C79–C80	178.4(4)
C77–C78–C79	176.7(4)
Fe4–C77–C78	177.9(3)

interest to note that both *syn* and *anti* conformers of the related complex $Cp(PPh_3)_2RuC{\equiv}CC{\equiv}CRu(PPh_3)_2Cp$ were X-ray characterized. Closest interactions in the *syn* conformers were outlined to be at the origin of minor distortions [26,27].

The ^{13}C-NMR resonances of the $-C_8-$ chain for the complex **2** were easily observed and summarized in Table 4 with the data reported for other $-C_8-$ chains with different organometallic termini [7,14,16,28]. The C_α resonances of these different compounds prove to be very sensitive to the nature of the terminal groups. In the (η^5-C_5Me_5)(dppe)Fe series, the C_α signals are shifted upfield from δ 99.7 to 143.2 ppm when the $-C_4-$ chain is replaced by the $-C_8-$ one. In the related (η^5-C_5Me_5)(PPh_3)(NO)Re–C_x–Re(NO)(PPh_3)(η^5-C_5Me_5) series, the C_α resonance is also shifted upfield when x increases from 4 ($\delta C_\alpha = 96.6$ ppm), to 8 ($\delta C_\alpha = 111.0$ ppm) and to 20 ($\delta C_\alpha = 127$ ppm) [16]. It is known that organic poly-ynes have an inductive electron-withdrawing effect, which acidity measurements show to decrease with the chain length [29]. In the organometallic complexes, as the length of the carbon chains increases, their electron-withdrawing effect on the metal increases

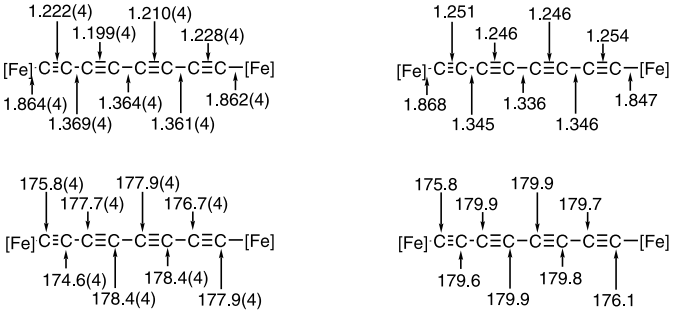

Plate 1. Experimental (left) and calculated (right) bond distances (Å) and angles (°) for the Fe–C_8–Fe assembly (**2**).

and induces an increased π-back-bonding response from the metal center, the intensity of which is strongly related to its electron richness. Related effects have been observed with the complexes (η^5-C_5Me_5)(dppe)FeC≡C-1,4-C_6H_4X, when X is an electron-withdrawing substituent (i.e. X = NO_2, CN) [21].

It is also noteworthy that the shifts of central carbon atoms are almost insensitive to the presence of the metal and to its electronic effect (Table 4). For these carbon atoms the ^{13}C chemical shifts are not are very different

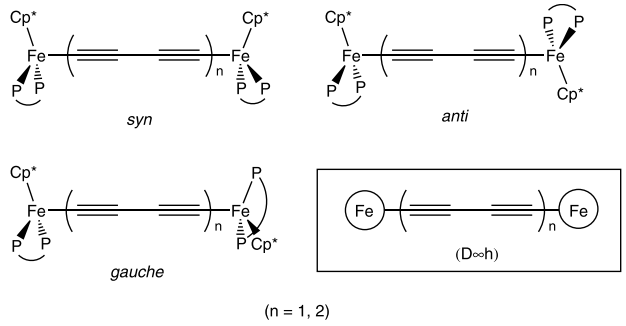

Scheme 2. Conformers of $(\eta^5\text{-}C_5Me_5)(dppe)Fe\text{–}(C{\equiv}C)_n\text{–}Fe(dppe)\text{-}(\eta^5\text{-}C_5Me_5)$.

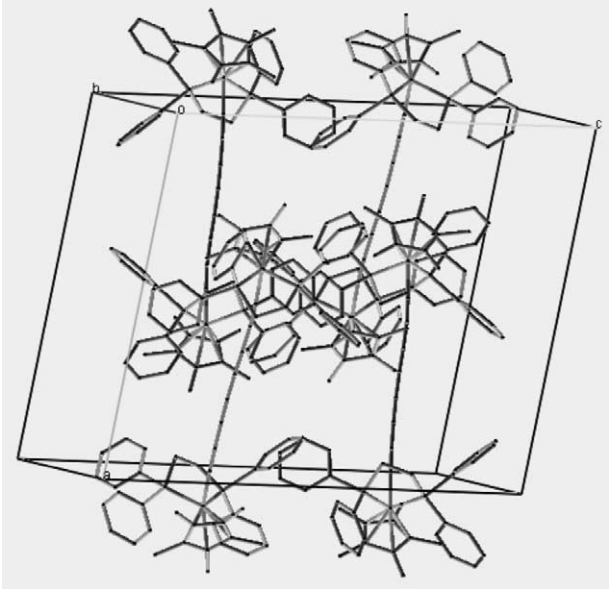

Fig. 2. Representative packing diagram for crystalline **2**.

Table 3
Comparison of the Fe–C and $C_\alpha{\equiv}C_\beta$ bond distances for **1**, **2** and the related iron complexes $(\eta^5\text{-}C_5Me_5)(CO)_2Fe\text{–}(C{\equiv}C)_n\text{–}Fe(CO)_2(\eta^5\text{-}C_5Me_5)$

Endgroup	*n*	Fe–C	$C_\alpha{\equiv}C_\beta$	Reference
$(C_5Me_5)(dppe)Fe$	2	1.884/1.889	1.220(3)/1.220(3)	[18]
$(C_5Me_5)(dppe)Fe$	4	1.862/1.864	1.222(4)/1.228(4)	This work
$(C_5Me_5)(CO)_2Fe$	1	1.929(9)	1.206(6)	[7]
$(C_5Me_5)(CO)_2Fe$	2	1.933(9)	1.197(4)/1.197(4)	[7]
$(C_5Me_5)(CO)_2Fe$	6	1.878(9)	1.23(1)/1.20(1)	[13]

from those found for organic poly-ynes [30,31]. These provide an indication that the valence bond formulations A and B (Scheme 3) should contribute to the description of the electronic structure of the [M]–$(C{\equiv}C)_n$–[M] compounds. As *n* increases, the weight of structure B increases when the metal ends are electron-rich, but this effect concerns mainly the carbon atoms

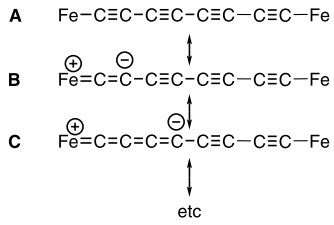

Scheme 3. Selected resonance structures for the Fe–C≡C–C≡C–C≡C–C≡C–Fe core.

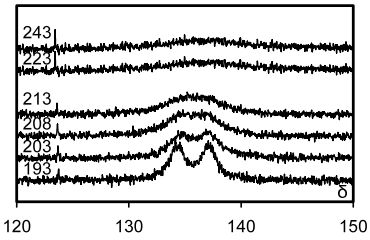

Fig. 3. Variable temperature (K) $^{31}P\{^1H\}$-NMR spectra for **1** in C_7D_8.

close to the metal centers and does apparently not propagate along the carbon chains. There is no experimental evidence to suggest a significant contribution of the structure C.

2.4. Vibrational spectroscopy

Given the rotational barrier observed for the diyne-diyl-bridged compound **1** and the steric congestion of the *syn* conformer, this complex should preferentially adopt the *anti* and *gauche* conformation (Scheme 2). In contrast, the octatetraynediyl-bridged **2** might exist as various conformers in solution [6,9]. Considering the different symmetries of these conformers, a close examination of the $\nu_{(C{\equiv}C)}$ characteristic bridge alkynyl stretching modes by means of infrared and Raman spectroscopy was initiated in order to get some information about the nature of the conformers possibly present in solution. A simple symmetry-based analysis reveals that all conformers exhibit 2*n* stretching modes (Scheme 2). For the *syn* and *gauche* isomers, all of them should be both infrared- and Raman-active. However, for the *anti* isomer, the exclusion rules tell us that only two of these will be infrared active (B_u symmetry), whereas the other two will be Raman-active (A_g symmetry).

The energy of the $\nu_{(C{\equiv}C)}$ stretching modes of the carbon-rich spacer detected by Raman and infrared are given in Table 5. Accordingly with the above analysis, the examination of the solid-state infrared spectra obtained from crystals for which the conformation of the molecules is known shows that all 2*n* absorptions ($n = 1$) are present for the *gauche* butadiyne-diyl complex **1**, whereas only half of the absorptions are observed for the *anti*-octatetrayne-diyl complex **2** ($n = 2$). Traces of the oxidized mixed-valence complex, characterized by

Table 4
^{13}C-NMR chemical shifts for selected M–C≡C–C≡C–C≡C–C≡C–M complexes

Endgroup	C_α	C_β	C_γ	C_δ	Reference
(C_5Me_5)(dppe)Fe	142.2	102.3	96.2	64.5	This work
$(C_5Me_5)(NO)(PPh_3)$Re	111.0	113.3	66.8	63.8	[16]
$(C_5Me_5)(CO)_2$Fe	110.8	94.8	61.6	51.4	[7]
$(C_5H_5)(CO)_3$W	112.4	91.6	63.7	60.9	[28]
$(C_6F_5)(P(p\text{-Tol})_3)_2$Pt	100.6	96.7	64.1	58.1	[14]

a peak at ca. 1879 cm^{-1} were always detected in *gauche*-**1**, even in samples made from microcrystals. Regarding the solid-state Raman spectra, as expected two absorptions are observed for *anti*-**2** and one of them is clearly distinct from these observed in the infrared spectrum (Fig. 4b). Apparently, one of the two symmetric (A_g) and one of the two antisymmetric (B_u) stretching modes of the octatetrayne-diyl bridge in *anti*-**2** absorb at very similar energies (ca. 2100 cm^{-1}), while the remaining ones can be identified at ca. 2000 cm^{-1} (B_u) and 1950 cm^{-1} (A_g), respectively. For *gauche*-**1**, however, the situation appears less straightforward. (i) First, there is not a strict correspondence between the energies of the intense Raman absorptions with these of the $\nu_{(C\equiv C)}$ modes detected by infrared (Fig. 4a). This can be rationalized considering that for complex **1**, the high-energy Raman absorption is split by Fermi-coupling (48 cm^{-1}) [20,32], often observed with this kind of Fe^{II} acetylide complexes. (ii) Then, while both stretching modes are in principle allowed for *gauche*-**1**, their intensities should be similar in the infrared and Raman. In fact, one of the absorptions largely dominates the other in infrared while the reverse situation results in Raman (Table 5). This indicate that the selection rule operative in the *anti* conformer is only partly relaxed in the *gauche* conformer, suggesting that the molecular (C_1) symmetry imposed by the organometallic end-groups in **1** is weakly sensed by the carbon-rich spacer. We can therefore attribute the high-energy absorption at ca. 2105 cm^{-1} to the "more symmetric" stretching mode and the other at ca. 1950 cm^{-1} to the "less symmetric" one.

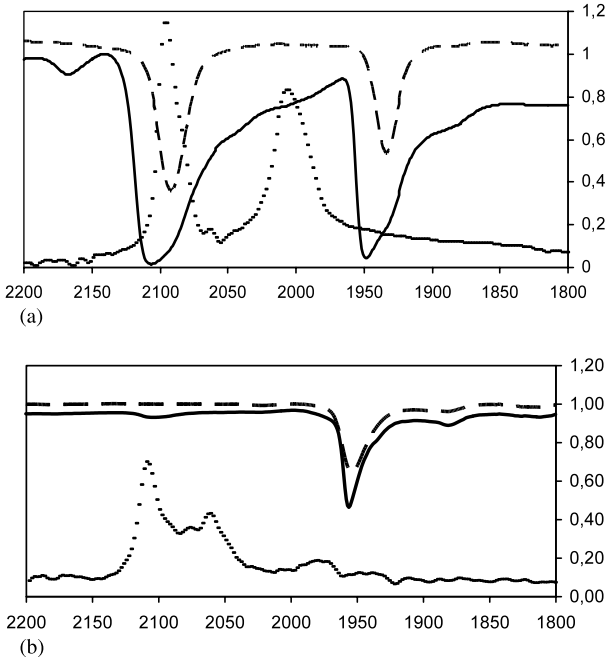

Fig. 4. IR and Raman spectra at 20 °C for **2** (a) and **1** (b), IR in KBr (—), IR in CH_2Cl_2 (- - -), and Raman spectra (. . .).

Comparison with the solution spectra obtained after dissolving the crystals in dichloromethane do not reveal any marked change in this spectral region, except a broadening of the solid state absorptions. Notably, no

Table 5
Raman/IR $\nu_{(C\equiv C)}$ data for (η^5-C_5Me_5)(dppe)Fe–$(C\equiv C)_n$–Fe(dppe)(η^5-C_5Me_5) (cm^{-1})

n	Method	ν_1	ν_2	ν_3	ν_4
1	IR/KBr [a]	2105 (br, vw)[1]	1956	–	–
	IR/CH_2Cl_2	–	1955	–	–
	IR/toluene	2102 (br, vw)	1955	–	–
	Raman [a]	2110, 2062	1981 (br, vw)	–	–
2	IR/KBr [a]	2107	–	–	1949
	IR/CH_2Cl_2	2092	–	–	1933
	IR/toluene	2101	–	–	1947
	Raman [a]	–	2096	2006	–

[a] This spectrum has been obtained from a single monocrystal.

absorption is detected for **2** around 2000 cm^{-1}. Additional absorptions in this energy range were expected for the *syn* and *gauche* conformers, since all the stretching modes of the polyyne bridge are in principle IR-active, according to the selection rules. Indeed, given that these conformers are present in solution of **2** (^{1}H- and ^{31}P-NMR reveals that the endgroups are freely rotating at ambient temperature) the ν_2 and ν_3 modes, exclusively Raman-active for the *anti*-conformer should now show-up. However, as observed for **1** in the solid state, the absorptions of the other conformers actually seem to obey to quite similar selection rules to those operative for the *anti* conformer of **2**. This also suggests that the selection rules for the vibronic transitions in these dinuclear compounds are mostly determined by the local $C_{\infty h}$ symmetry of the bridge, with Σ_g^+ modes being Raman-active and Σ_u^+ modes infrared-active, rather than by the molecular symmetry of a given conformer.

2.5. Electronic spectroscopy

Solutions of the complexes **1** and **2** turn from orange to red as the length of the carbon chains increases. As shown in Table 6, the complex **2** absorbs over the entire visible range reflecting a multitude of transitions. The two highest energy bands can be attributed to intraligand (IL) $\pi \rightarrow \pi^*$ transitions of the (η^5-C_5Me_5) and dppe ligands. These bands which are characteristic of the (η^5-C_5Me_5)Fe(dppe) organometallic end-capping groups, are not present in the spectrum of the 1,8-bis(triethylsilyl)octatetrayne (**2***) [33] and their energies and intensities weakly depend on the number of atom on the carbon chain.

With reference to the electronic absorption studies of monometallic complexes with carbon chain ligands like (η^5-C_5Me_5)(dppe)Fe–C≡CC≡CSiMe$_3$ (**5**) [20] and (η^5-C_5Me_5)(dppe)Ru–C≡CC≡CSiMe$_3$ (**6**) [34], which show low energy absorptions in the range 340–450 nm, the low energy absorptions observed in the spectra of **2** and **1** are tentatively attributed to $d\pi Fe \rightarrow \pi^*(C{\equiv}C)$ metal-to-ligand charge transfer transitions (MLCT). This assignment is also supported by the observation of only two bands for the organic compound **2*** for which only $\pi \rightarrow \pi^*$ transitions can be observed. As the number of –C≡C– fragments increases from 2 to 4, the bands are red-shifted and their number and their intensities are increased. Assignment of these bands is provided below on the basis of theoretical calculations. Few data on the electronic absorption spectra are available for the complexes [M]–$(C{\equiv}C)_n$–[M] in the literature. Absorption bands at 310 and 337 nm which could be attributed to the MLCT transitions have been observed in Cp(PPh$_3$)$_2$RuC≡CC≡CRu(PPh$_3$)$_2$Cp and Cp(PPh$_3$)(PMe$_3$)RuC≡CC≡CRu(PMe$_3$)(PPh$_3$)Cp, respectively.

Table 6
UV–vis absorption bands for **1**, **2** and the related compounds in CH_2Cl_2

Compound	λ (nm) ($\varepsilon \pm 10\%$ in $M^{-1}\,cm^{-1}$)
1 [a]	232 (157000); 272 (sh, 66400); 364 (8700); 554 (sh, 660)
2 [a]	232 (157000); 260 (sh, 86000); 390 (71000); 494 (sh, 5100); 707 (90)
2* [b]	316 (398000); 336 (447000)
5 [c]	287 (27000); 371 (sh, 3300); 424 (sh, 1500)
6 [c]	257 (44000); 345 (sh, 5000);
7 [d]	232 (65000); 270 (31000); 346 (20500)
8 [e]	234 (58000); 262 (58000); 340 (56000); 360 (67000); 390 (60000)
9 [e]	228 (78000); 384 (110000); 430 (130000); 466 (190000); 508 (140000); 582 (73000); 602 (73000)

[a] This work.
[b] From Ref. [33].
[c] From Ref. [34].
[d] From Ref. [9].
[e] From Ref. [16].

The electronic transitions observed for **1** and **2** can also be compared with the series of complexes [(η^5-C_5Me_5)(PPh$_3$)(NO)Re]–$(C{\equiv}C)_n$–[Re(NO)(PPh$_3$)(η^5-C_5Me_5)] ($n = 2$, **7**; $n = 4$, **8**; $n = 20$, **9**) for which the UV–vis spectra were recorded (see Table 6) [9,16]. The data summarized in Table 6 show that the number of transitions, their intensities and their energies, depends on the nature of the terminal organometallic ends. It is also noteworthy that for the iron complexes, the intensity of the bands decreases with their energy, whereas it was pointed out that the MLCT transition located at the highest energy is never the most intense in the rhenium series [16].

2.6. Mössbauer spectroscopy

^{57}Fe Mössbauer spectroscopy can shed some light on the nature of the bonding between the iron center and the all-carbon chain. Indeed, the isomeric shift (δ) provides a rough indication of the electronic density at the iron nucleus and the width of the quadrupole doublet (QS) depends on several parameters including the oxidation state of the iron atom and the anisotropic electron distribution in the valence shell of the Mössbauer atom [35]. Therefore, one can expect that for a given oxidation state, the variation of the QS value mainly depends on the Fe–C bond strength when the other ancillary ligands remain unchanged [36]. The zero-field ^{57}Fe Mössbauer spectrum of the complex **2** was obtained at 80 K and compared with that of **1**. The spectrum of each of these compounds shows a unique doublet and the fitting parameters were computed. The isomeric shift δ of the complex **2** ($\delta = 0.24$ mm s^{-1}) appears slightly smaller than in the FeC_4Fe compound **1** ($\delta = 0.27$ mm s^{-1}) indicating that the electronic density at the iron nucleus is slightly smaller in **2** than in **1**. This

is corroborated by the redox potentials and in agreement with an electron-withdrawing effect of the carbon chains which increases with the chain length. At this stage, it can be recalled that the CV of **2** displays two well-reversible redox processes ($E_1^0 = -0.23$ and $E_2^0 = 0.20$). The large wave separation indicates a strong electronic coupling between the iron centers, in agreement with the value determined from the analysis of the NIR spectrum of the corresponding mixed-valence complex $\mathbf{2}^+$ ($V_{ab} = 0.32$ eV). This is the largest electronic coupling never reported through nine bounds [18].

In addition, the QS values determined for the C_n-bridged complexes **1** and **2**, are close to 2.0 mm/s and are typical of the iron(II) oxidation state in this series of compounds. In the case of the C_8-bridged compound **2** the value of QS (1.94 mm s^{-1}) is significantly smaller than the QS parameter (2.07 mm s^{-1}) obtained previously for its homologue **1**. In many examples taken in the $(\eta^5\text{-}C_5Me_5)(dppe)Fe^{II}$ series, we found that the decrease of the QS values is associated with the decrease of the Fe–C bond distances [36]. The decrease of the QS parameters with the increase of the carbon chain length also constitutes another spectroscopic indication for an increase Fe–C bond order in **2** with respect to **1**.

2.7. Computational results

Density functional (DF) molecular orbital (MO) calculations were carried out on the hydrogen-substituted model complex $(\eta^5\text{-}C_5H_5)(\eta^2\text{-dpe})Fe{-}C{\equiv}C{-}C{\equiv}C{-}C{\equiv}C{-}C{\equiv}C{-}Fe(\eta^5\text{-}C_5H_5)(\eta^2\text{-dpe})$ (**2-H**; dpe = $H_2P{-}(CH_2)_2{-}PH_2$) to further the understanding of the geometry and the electronic structure of the C_8-containing compound **2**. Similar calculations were performed again on the previously studied model complex $(\eta^5\text{-}C_5H_5)(\eta^2\text{-dpe})Fe{-}C{\equiv}C{-}C{\equiv}C{-}Fe(\eta^5\text{-}C_5H_5)(\eta^2\text{-dpe})$ (**1-H**) [17] used to mimic the C_4-containing compound **1**, in order to understand the effect of the lengthening of the carbon linker on the electronic properties. Computational details are given in Section 3.

The optimized geometries of both models compare rather well with their corresponding X-ray structures (see Plates 1 and 2). The dihedral angle $Fe{-}C_\alpha{-}C'_\beta{-}Fe'$ in **2-H** is 179.6°, giving the *anti* configuration as the most stable arrangement, in agreement with the X-ray structure. Nevertheless, the energy of *syn* and *gauche* conformations are computed slightly larger. The *syn* and *gauche* conformers lie above the *anti* by around 1.0 and 1.5 kJ mol^{-1}, respectively.

The largest bond distance deviation (0.04 Å) between the experimental and optimized structures of **2** and **2-H** concerns the C≡C triple bonds of the C_8 chain (see Plate 1). Such a deviation between the theory and experiment is typical for this kind of carbon chain-containing organometallic compounds [10,17]. The weak bending along the $Fe{-}C_8{-}Fe$ backbone observed in **2** is reproduced at remarkably high accuracy in **2-H** (see Plate 1). The lengthening of the conjugated carbon chain from C_4 to C_8 leads to some contraction of the Fe–C bond distances from 1.917 to 1.867 Å in the models. This is in agreement with experiment which shows a shortening of 0.024 Å in average for the Fe–C bond distances going from **1** to **2** (see above). The C–C triple bonds are calculated slightly longer in **2-H** than in **1-H**, whereas a slight shortening of the single bonds is computed when the number of carbon atoms in the chain increases, as observed experimentally. This could reflect some increase of the cumulenic character upon lengthening of the conjugated chain.

The DF-MO diagram of **2-H** is shown on the right-hand side of Fig. 5. For comparative purposes, the DF-MO diagram of **1-H** is recalled on the left-hand side of Fig. 5. The MO diagram of **2-H** is qualitatively similar to that of the hypothetical model $\{Ru(dpe)Cp\}_2(\mu\text{-}C_8)$ recently reported with a rather large energy gap separating the occupied and vacant orbital sets (1.64 eV) and HOMO and HOMO-1 highly delocalized all over the $Fe{-}C_8{-}Fe$ backbone, well-separated from the rest of the occupied orbitals [37].

As shown in Fig. 6, these HOMO and HOMO-1 are π-type in character and antibonding between Fe and C(1), C(2) and C(3), and C(4) and C(4′), bonding between C(1) and C(2) and C(3) and C(4), and nonbonding between C(4) and C(4′). These MOs are both Fe (26 and 21%) and C (63 and 68%) in character and result from antibonding interactions between dπ orbitals of the iron fragments and in-plane ($\pi_\parallel$) and out-of-plane ($\pi_\perp$) π-orbitals of the octatetraynediyl group. This is a common feature for carbon group-containing organometallic species [10,17].

Surprisingly enough, the HOMOs of the C_8-containing complex **2-H** lie at substantially lower energy than the HOMOs of the C_4-containing complex **1-H** (see Fig. 5). This leads to a larger energy gap separating them from the LUMOs which, in both cases, are metal–ligand (Cp and dpe) antibonding in character. The nature and the nodal properties of the HOMOs do not significantly change upon the lengthening of the carbon linker. However, a comparison of the metal vs. carbon percen-

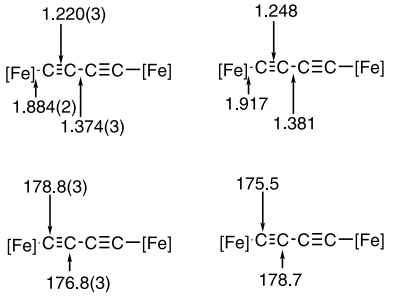

Plate 2. Experimental (left) and calculated (right) bond distances (Å) and angles (°) for the $Fe{-}C_4{-}Fe$ assembly (**1**).

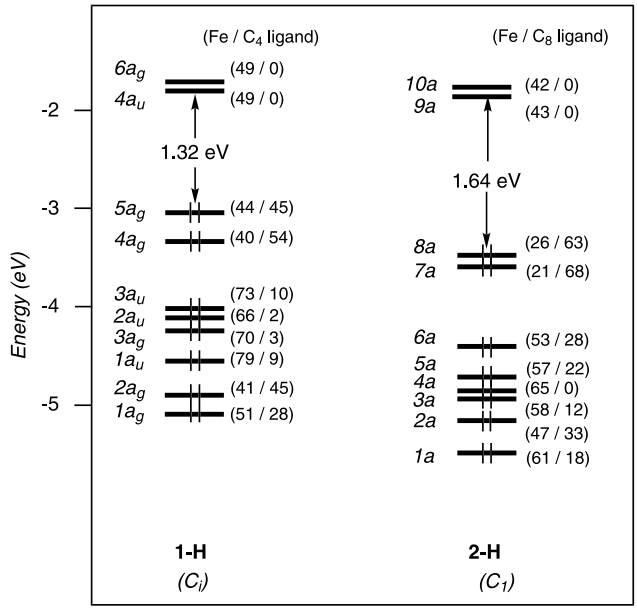

Fig. 5. DFT MO diagrams of **1-H** (left) and **2-H** (right). The metal/carbon chain percentage contributions of the MOs are given in brackets.

tage contribution reveals that the lengthening of the carbon chain yields HOMOs less heavily weighted on the metal centers (see Fig. 5). This is due to a weaker antibonding interaction between the latter and the C(α) atoms of the carbon bridge. Consequently, oxidation will affect more deeply the carbon chain in **2-H** than **1-H**.

First excitation energies (up to 250 nm) were calculated for **1-H** and **2-H** in order to get a better understanding of the experimental electronic spectra. For **1-H**, only one transition at 284 nm has significant oscillator strength (0.176) and thus can be unambiguously attributed to the UV–visible band observed experimentally at 272 nm. This transition corresponds to a combined excitation from the HOMO and HOMO-1 to high-lying antibonding unoccupied orbitals localized on the Cp ligands and the carbon chain (LUMO+8/+12). The main absorptions calculated for **2-H** are found at 304 and 344 nm (oscillator strengths 0.190 and 0.194, respectively). The character of these transitions is somewhat different to what is found for **1-H**. The less energetic transition corresponds to an excitation from the HOMO-1 to an orbital localized over the C_8 chain and the dpe ligands (LUMO+9). The second transition is an excitation from a low-lying metallic orbital (HOMO-7) to the LUMO+3, fully localized on the carbon chain spacer. Two bands are also observed experimentally in that region of the spectrum at 260 and 390 nm. The discrepancies between experimental and calculated values are mainly due to the structural simplification performed on **1** and **2** to reduce the computational effort. Nevertheless, the theoretical results provide a reliable assignation to the main absorption observed. It has to be noted that the HOMO–LUMO excitations are calculated around 1000 nm for **1-H** and 800 nm for **2-H** (oscillator strength < 0.002) and were not experimentally observed.

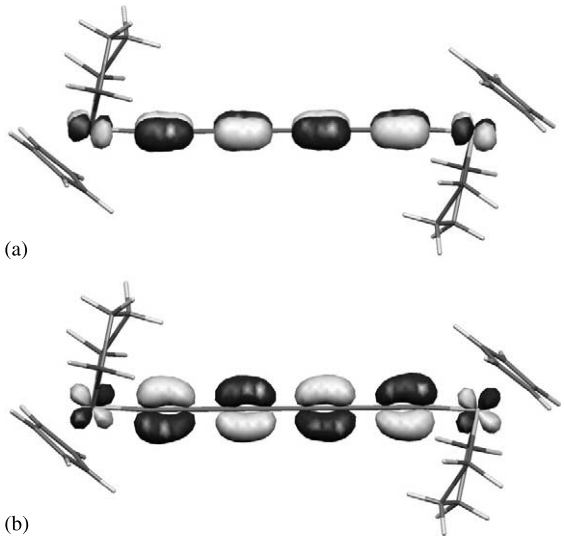

Fig. 6. Isosurfaces of the two highest occupied MOs of selected (η^5-C_5H_5)(η^2-dpe)Fe–(C ≡ C)$_4$–Fe(η^5-C_5H_5)(η^2-dpe). (a) HOMO and (b) HOMO-1 (contour value: 0.05 a.u.).

3. Conclusions

In the [Fe]–(C≡C)$_n$–[Fe] series, X-ray analyses show an increase of the cumulenic character of the all-carbon chains with the number of carbon in the chain. The ^{13}C-NMR, Mössbauer spectroscopy and theoretical calculations confirm this trend both in solution and in the solid state. In addition, the cumulenic-type structure is more pronounced in the vicinity of the metal than in the middle of the all-carbon fragment. In the complex **2**, the rotation of the end-capping metal ends is free and the different conformers are very close in energy as shown by the DFT calculations on the model compound **2-H**. Vibrational spectroscopy studies established that the selection rules for the vibronic transitions in **1** and **2** are mostly determined by the local $C_{\infty h}$ symmetry of the bridge rather than by the molecular symmetry of a given conformer. Transitional spectroscopy shows that the number of transitions and their energies depend on the length of the all-carbon chains and the nature of the metal ends. Analysis of the spectra is complex and the calculations clearly indicate that the HOMO–LUMO gaps cannot be determined from the UV–vis spectra. They were calculated around 1000 and 800 nm for **1-H** and **2-H**, respectively, in accord with an increase of the gap with the carbon chain length.

4. Experimental

4.1. General data

All manipulations were carried out under inert atmosphere. Solvents or reagents were used as follows: Et_2O, THF and *n*-pentane, distilled from Na/benzophenone; CH_2Cl_2, distilled from CaH_2 and purged with argon; complexes (η^5-C_5Me_5)(dppe)Fe(C≡CC≡CSiMe$_3$) (**3**) [19] and (η^5-C_5Me_5)(dppe)Fe(C≡CC≡CH) (**4**) [20] were prepared by previously published procedures. High-field NMR spectra experiments were performed on multinuclear Bruker 300 or 200 MHz instruments (AM300WB and 200DPX, respectively). Chemical shifts are given in ppm relative to internal tetramethylsilane (TMS) for ^{1}H-and ^{13}C-NMR spectra, external H_3PO_4 for ^{31}P-NMR spectra. Conformational analysis was carried out with CHEM-3D 6.0 for Windows from Cambridge Soft. Transmittance-FTIR and Raman spectra were recorded using a Bruker IFS28 spectrometer (400–4000 cm^{-1}). UV–vis spectra were recorded on an UVIKON 942 spectrometer. Mössbauer spectra were recorded with a 2.5×10^{-2} C (9.25×10^8 Bq) ^{57}Co source using a symmetric triangular sweep mode at LCC (Toulouse) [38]. LSI-MS analyses were effected at the Centre Regional de Mesures Physiques de l'Ouest (CRMPO, Rennes, France) on a high resolution MS/MS ZabSpec TOF Micromass spectrometer (8 kV). Elemental analyses were performed at the Centre for Microanalysis of the CNRS at Lyon-Solaise, France.

4.2. Synthesis of 2

A Schlenk tube was charged with FeC_4H (0.250 g, 0.39 mmol), $Cu(OAc)_2$ (0.070 g, 0.39 mmol), DBU (0.060 g, 0.39 mmol) and 10 ml of pyridine. The mixture was stirred at 45 °C for 3 h. The solvent was removed under oil-pump vacuum. The residue was washed with diethyl ether (5 ml) and toluene (2 ml) before being dissolved in dichloromethane and filtered through a 2 × 4 cm celite column. The solution was concentrated to 2 ml and addition of diethyl ether (10 ml) gave **2** as a red powder (0.200 g, 80%). Anal. Calc. for $C_{80}H_{78}Fe_2P_4 \cdot 0.25CH_2Cl_2$: C, 74.36; H, 6.10. Found: C, 74.34; H, 6.09%. MS: calculated for **2** 1274.4. Found: 1274.0. NMR: ^{1}H (300 MHz, C_6D_5Br, 25 °C): 7.81–7.11 (m, 40 H, Ph); 2.45–1.79 (2m, 8H, CH_2); 1.35 (s, 30 H, $C_5(CH_3)_5$) ppm. ^{13}C{^{1}H} (75 MHz, C_6D_5Br, 25 °C): 139.5 (t, $^2J_{PC} = 42$ Hz, FeC); 138.3–127.2 (m, Ph); 101.8 (s, Fe*C*C); 88.4 (s, $C_5(CH_3)_5$); 62.7 (t, $^4J_{PC} = 3$ Hz, FeCC*C*); 50.6 (s, FeCCC*C*); 30.5 (m, CH_2); 9.9 (s, $C_5(CH_3)_5$) ppm. ^{31}P{^{1}H} (121 MHz, C_6D_5Br, 25 °C) 98.5 (s) ppm.

4.3. Crystallography

Data were collected on crystals of **2** as summarized in Table 1 [39,40]. Cell constants and an orientation matrix of **2** were obtained from a least-squares refinement using 25 high θ reflections. After Lorentz and polarization corrections and absorption corrections (φ-scans) [41], the structure was solved with SIR-97 [42], which revealed the non-hydrogen atoms. After anisotropic refinements, a Fourier difference map revealed many hydrogen atoms. Atomic scattering factors were taken from the literature [43]. A Silicon Graphics Indy computer with the MOLEN package (ENRAF-Nonius, 1990) was used for structure determination [39]. Ortep views were generated with PLATON-98 [44]. All calculations were performed on a Pentium NT Server computer.

4.4. Computational details

DFT calculations were carried out using the Amsterdam Density Functional (ADF) program.[45–47] The model compounds **1-H** and **2-H** were used in order to reduce computational effort. Electron correlation was treated within the local density approximation (LDA) in the Vosko–Wilk–Nusair parameterization. [48] The nonlocal corrections of Becke [49] and of Perdew [50] were added to the exchange and correlation energies, respectively. The numerical integration procedure applied for the calculations was developed by Te Velde et al. [45,51] The basis set used for the metal atoms was a triple-ζ slater-type orbital (STO) basis for Fe 3d and 4s, and a single-ζ function for 4p. A triple-ζ STO basis set was employed for 1s of H, 2s and 2p of C, and 3s and 3p of P, extended with a single-ζs polarization function (2p for H; 3d for C and P). Full geometry optimization (assuming C_1 symmetry) was carried out on **2-H**, **1-H** was optimized in C_i symmetry accordingly with the experimental results, using the analytical gradient method implemented by Verluis and Ziegler [52]. Time-dependant density functional theory (TD-DFT) calculations were performed on the optimized structures using the LB94 functional [53]. The excitation energies and oscillator strengths were calculated following the procedure described by van Gisbergen et al. [53]. The representations of the MOs were done using MOLEKEL4.1 [54].

5. Supplementary material

Crystallographic data for the structural analysis have been deposited with the Cambridge Crystallographic Data Centre, CCDC No. 210924 for compound **2**. Copies of this information may be obtained free of charge from The Director, CCDC, 12 Union Road,

Cambridge CB2 1EZ, UK (Fax: 44-1223-336033; e-mail: deposit@ccdc.cam.ac.uk or www: http://www.ccdc.cam.ac.uk).

Acknowledgements

J.-P. Guégan is acknowledged for his skilful assistance in low-temperature NMR measurements. This paper was written in March 2003 during a visit at the University of Adelaide. C.L. is grateful to the CNRS and ARC-IREX program for supporting this visit and to Professor M.I. Bruce for his kind hospitality and helpful discussions.

References

[1] F. Paul, C. Lapinte, Coord. Chem. Rev. 178–180 (1998) 427.
[2] M.D. Ward, Chem. Soc. Rev. (1995) 121.
[3] S. Barlow, D. O'Hare, Chem. Rev. 97 (1997) 637.
[4] V. Grosshenny, A. Harriman, M. Hissler, R. Ziessel, Platinum Met. Rev. 40 (1996) 26.
[5] M.I. Bruce, Coord. Chem. Rev. 166 (1997) 91.
[6] F. Paul, C. Lapinte, in: M. Gielen, R. Willem, B. Wrackmeyer (Eds.), Unusual Structures and Physical Properties in Organometallic Chemistry, Wiley, London, 2002, p. 220.
[7] M. Akita, M.-C. Chung, A. Sakurai, S. Sugimoto, M. Terada, M. Tanaka, Y. Moro-oka, Organometallics 16 (1997) 4882.
[8] N. Le Narvor, L. Toupet, C. Lapinte, J. Am. Chem. Soc. 117 (1995) 7129.
[9] M. Brady, W. Weng, Y. Zhou, J.W. Seyler, A.J. Amoroso, A.M. Arif, M. Böhme, G. Frenking, J.A. Gladysz, J. Am. Chem. Soc. 119 (1997) 775.
[10] M.I. Bruce, P.J. Low, K. Costuas, J.-F. Halet, S.P. Best, G.A. Heath, J. Am. Chem. Soc. 122 (2000) 1949.
[11] S. Kheradmandan, K. Heinze, H.W. Schmalle, H. Berke, Angew. Chem. Int. Ed. Engl. 38 (1999) 2270.
[12] V.W.-W. Yam, V.C.-Y. Lau, K.-K. Cheung, Organometallics 15 (1996) 1740.
[13] A. Sakurai, M. Akita, Y. Moro-oka, Organometallics 18 (1999) 3241.
[14] W. Mohr, J. Stahl, F. Hampel, J.A. Gladysz, Inorg. Chem. 40 (2001) 3263.
[15] R.D. Adams, B. Qu, M.D. Smith, Organometallics 21 (2002) 3867.
[16] R. Dembinski, T. Bartik, B. Bartik, M. Jaeger, J.A. Gladysz, J. Am. Chem. Soc. 122 (2000) 810.
[17] H. Jiao, K. Costuas, J.A. Gladysz, J.-F. Halet, M. Guillemot, L. Toupet, F. Paul, C. Lapinte, J. Am. Chem. Soc. 125 (2003) 9511.
[18] F. Coat, C. Lapinte, Organometallics 15 (1996) 477.
[19] F. Coat, P. Thominot, C. Lapinte, J. Organomet. Chem. 629 (2001) 39.
[20] F. Coat, M.-A. Guillevic, L. Toupet, F. Paul, C. Lapinte, Organometallics 16 (1997) 5988.
[21] R. Denis, L. Toupet, F. Paul, C. Lapinte, Organometallics 19 (2000) 4240.
[22] R. Dembinski, T. Lis, S. Szafert, C.L. Mayne, T. Bartik, J.A. Gladysz, J. Organomet. Chem. 578 (1999) 229.
[23] J. Marina, K.D. John, M.D. Hopkins, Adv. Organomet. Chem. 38 (1995) 80.
[24] D.L. Lichtenberger, S.K. Renshaw, R.M. Bullock, J. Am. Chem. Soc. 115 (1993) 3276.
[25] B. Bartik, R. Dembinski, T. Bartik, A.M. Arif, J.A. Gladysz, New J. Chem. 21 (1997) 739.
[26] M.I. Bruce, P. Hinterding, E.R.T. Tiekink, B.W. Skelton, A.H. White, J. Organomet. Chem. 450 (1993) 209.
[27] M.I. Bruce, F.S. Wong, B.W. Skelton, A.H. White, J. Chem. Soc. Dalton Trans. (1981) 1398.
[28] M.I. Bruce, M. Ke, P.J. Low, J. Chem. Soc. Chem. Commun. (1996) 2405.
[29] R. Eastmond, T.R. Johnson, D.R.M. Walton, J. Organomet. Chem. 50 (1973) 87.
[30] G. Schermann, T. Grösser, F. Hample, A. Hirsch, Chem. Eur. J. 3 (1997) 1105.
[31] R.J. Lagow, J.J. Kampa, H.-C. Wei, S.L. Battle, J.W. Genge, D.A. Laude, C.J. Harper, R. Bau, R.C. Stevens, J.F. Haw, E. Munson, Science 267 (1995) 362.
[32] F. Paul, J.-Y. Mevellec, C. Lapinte, J. Chem. Soc. Dalton Trans. (2002) 1783.
[33] R. Eastmond, T.R. Johnson, D.R. Walton, Tetrahedron 28 (1972) 4601.
[34] M.I. Bruce, B.E. Ellis, C. Lapinte, in preparation.
[35] P. Gütlich, R. Link, A. Trautwein, Mössbauer Spectroscopy and Transition Metal Chemistry, vol. 3, Springer-Verlag, Berlin, 1978.
[36] G. Argouarch, P. Thominot, F. Paul, L. Toupet, C. Lapinte, C. R. Chim. 6 (2003) 209.
[37] M.I. Bruce, J.-F. Halet, B. Le Guennic, B.W. Skelton, A.H. White, Inorg. Chim. Acta 350 (2003) 175.
[38] N.N. Greenwood, Mössbauer Spectroscopy, Chapman & Hall, London, 1971.
[39] C.K. Fair, MOLEN: An Interactive System for Crystal Structure Analysis, Enraf-Nonius, Delft, The Netherlands, 1990.
[40] Nonius, Kappa CCD Software, Nonius BV, Delft, The Netherlands, 1999.
[41] A.L. Spek, HELENA: Program for the Handling of CAD4-Diffractometer Output SHELX(S/L), Utrecht University, Utrecht, The Netherlands, 1997.
[42] Z. Otwinowski, W. Minor, Processing of X-ray diffraction data collected in oscillation mode, in: C.W. Carter, R.M. Sweet (Eds.), Methods in Enzymology. Macromolecular Crystallography, Part A, Academic Press, London, 1997, pp. 276–307.
[43] A.J.C. Wilson (Ed.), International Tables for X-ray Crystallography, Vol. C, Kluwer Academic Publishers, Dordrecht, 1992.
[44] A. Altomare, M.C. Burla, M. Camali, G. Cascarano, C. Giacovazzo, A. Guagliardi, A.G.G. Moliterni, G. Polidori, R. Spagna, SIR-97: a new tool for crystal structure determination and refinement, J. Appl. Crystallogr. 31 (1998) 74.
[45] G. Te Velde, F.M. Bickelhaupt, S.J.A. van Gisbergen, C. Fonseca Guerra, E.J. Baerends, J.G. Snijders, T.J. Ziegler, Comput. Chem. 22 (2001) 931.
[46] C. Fonseca Guerra, J.G. Snijders, G. te Velde, E.J. Baerends, J. Theor. Chem. Acc. 99 (1998) 391.
[47] S. ADF2.3 and ADF2002.01, Theoretical Chemistry, Vrije Universiteit, Amsterdam, The Netherlands. Available at: http://www.scm.com.
[48] S.D. Vosko, L. Wilk, M. Nusair, Can. J. Chem. 58 (1990) 1200.
[49] A.D. Becke, Phys. Rev. A 38 (1988) 3098.
[50] J.P. Perdew, Phys. Rev. B 34 (1986) 7406.
[51] G. Te Velde, E.J. Baerends, J. Comput. Phys. 99 (1992) 84.
[52] L. Verluis, T. Ziegler, J. Chem. Phys. 88 (1988) 322.
[53] S.J.A. van Gisbergen, J.G. Snijders, E.J. Baerends, Comput. Phys. Commun. 118 (1979) 119.
[54] H.P. Lüthi, S. Portmann, J. Weber, F. MOLEKEL4.1 P., Swiss Center for Scientific Computing (CSCS), Manno, Switzerland, 2000–2001.